Journal of Computational Physics 228 (2009) 3421–3432

Contents lists available at ScienceDirect

Journal of Computational Physics

journal homepage: www.elsevier.com/locate/jcp

A discrete action principle for electrodynamics and the construction of explicit symplectic integrators for linear, non-dispersive media

Jeffrey M. McMahon [a,b,*], Stephen K. Gray [b], George C. Schatz [a]

[a] Department of Chemistry, Northwestern University, 2145 Sheridan Road, Evanston, IL 60208, USA
[b] Chemical Sciences and Engineering Division, Argonne National Laboratory, Argonne, IL 60439, USA

ARTICLE INFO

Article history:
Received 19 June 2008
Received in revised form 14 January 2009
Accepted 20 January 2009
Available online 29 January 2009

MSC:
65M12
65P10
65Z05
70S05
78M20

Keywords:
Dispersion
Electrodynamics
FDTD
Lagrangian
Runge–Kutta
Stability
Symplectic integrator

ABSTRACT

In this work, we derive a discrete action principle for electrodynamics that can be used to construct explicit symplectic integrators for Maxwell's equations. Different integrators are constructed depending on the choice of discrete Lagrangian used to approximate the action. By combining discrete Lagrangians in an explicit symplectic partitioned Runge–Kutta method, an integrator capable of achieving any order of accuracy is obtained. Using the von Neumann stability analysis, we show that the integrators greatly increase the numerical stability and reduce the numerical dispersion compared to other methods. For practical purposes, we demonstrate how to implement the integrators using many features of the finite-difference time-domain method. However, our approach is also applicable to other spatial discretizations, such as those used in finite element methods. Using this implementation, numerical examples are presented that demonstrate the ability of the integrators to efficiently reduce and maintain a minimal amount of numerical dispersion, particularly when the time-step is less than the stability limit. The integrators are therefore advantageous for modeling large, inhomogeneous computational domains.

1. Introduction

Many numerical methods have been developed to simulate the dynamics of electromagnetic fields, such as the finite-difference time-domain (FDTD) method [1,2] and the time-domain finite element method (TD-FEM) [3]. Typically these methods integrate Maxwell's equations by approximating the time derivatives with second-order accurate Taylor expansions. These integration methods, along with the spatial discretization, can lead to significant numerical dispersion [2,3], where waves propagate with a wavelength dependent velocity through the computational domain. This causes phase errors, pulse broadening, as well as other problems. In order to reduce the numerical dispersion, higher order approximations to the derivatives are often used. In the context of FDTD, these methods are typically applied to the spatial derivatives [4]. However, they can also be applied to the time derivatives [5], as long as care is taken so that the dynamical invariants of the problem

* Corresponding author. Address: Department of Chemistry, Northwestern University, 2145 Sheridan Road, Evanston, IL 60208, USA. Tel.: +1 630 252 9861; fax: +1 847 491 7713.
E-mail address: jeffrey-mcmahon@northwestern.edu (J.M. McMahon).

0021-9991/$ - see front matter © 2009 Elsevier Inc. All rights reserved.
doi:10.1016/j.jcp.2009.01.019

(e.g. the energy density) are preserved. One type of time integrator that preserves dynamical invariants up to a desired order of accuracy is a symplectic integrator (SI) [6–19]. SIs for Maxwell's equations have appeared before [20–22] in the context of Hamiltonian mechanics. Some of these schemes [20–22] have been derived using a "helicity" Hamiltonian [23], which is not the physical energy density, but nonetheless is equivalent to Maxwell's equations. However, it is of interest to develop numerical approaches based on physical premises so they can be easily extended to more complex situations, such as the coupling of electromagnetics with quantum mechanics [24]. Another scheme [21] was derived using a physical Hamiltonian. However, the SIs developed have limited applicability due to the constraints imposed on the Hamiltonian. In this paper, we take a different approach and use Lagrangian mechanics to derive a discrete action principle for electrodynamics that can be used to construct a variety of SIs. Our approach is based on the discrete variational integration ideas developed by Marsden and West [25], which have recently been applied by Qin and Guan to describe charged particle motion in magnetic fields [26]. We extend their ideas from particle Lagrangian mechanics to a field theory in terms of a Lagrangian density [7]. We then use the physically correct Lagrangian density to develop SIs for a larger class of problems in electrodynamics than possible using previous approaches. Even though the Lagrangian density is in terms of potentials, we show that the integrators, after construction, can easily be expressed and implemented entirely in terms of fields.

The structure of this paper is as follows: in Section 2, we review Maxwell's equations and extend the discrete action principle to a field theory; in Section 3, we construct SIs for Maxwell's equations, including an integrator capable of achieving any order of accuracy; the numerical stability and dispersion of the SIs are analyzed in Section 4; practical implementation of the SIs using FDTD techniques is discussed in Section 5; in Section 6, we present numerical examples; lastly, a summary and conclusions are given in Section 7.

2. A discrete action principle for electrodynamics

The dynamics of electromagnetic fields are described by Maxwell's equations, which in differential form for a linear medium are

$$\varepsilon \frac{\partial}{\partial t}\vec{E} = \frac{1}{\mu}\vec{\nabla}\times\vec{B} - \vec{J}, \tag{1}$$

$$\frac{\partial}{\partial t}\vec{B} = -\vec{\nabla}\times\vec{E}, \tag{2}$$

$$\vec{\nabla}\cdot(\varepsilon\vec{E}) = \rho, \tag{3}$$

$$\vec{\nabla}\cdot\vec{B} = 0, \tag{4}$$

where $\vec{E}$ and $\vec{B}$ are the electric and magnetic fields, ε and μ are the permittivity and permeability of the medium, and $\vec{J}$ and ρ are the current and charge densities.

Lagrangian mechanics can also be used to describe the dynamics of electromagnetic fields, by using the vector ($\vec{A}$) and scalar (ϕ) potentials, which are related to $\vec{E}$ and $\vec{B}$ by

$$\vec{B} = \vec{\nabla}\times\vec{A}, \tag{5}$$

$$\vec{E} = -\frac{\partial}{\partial t}\vec{A} - \vec{\nabla}\phi. \tag{6}$$

The Lagrangian density, L, for the electromagnetic field is expressed as

$$L = \frac{\varepsilon}{2}\vec{E}\cdot\vec{E} - \frac{1}{2\mu}\vec{B}\cdot\vec{B} + \vec{J}\cdot\vec{A} - \rho\phi \tag{7}$$

or

$$L = \frac{\varepsilon}{2}\left|\frac{\partial}{\partial t}\vec{A} + \vec{\nabla}\phi\right|^2 - \frac{1}{2\mu}|\vec{\nabla}\times\vec{A}|^2 + \vec{J}\cdot\vec{A} - \rho\phi, \tag{8}$$

where L is a function of $\vec{A}$, $\partial\vec{A}/\partial t$, and ϕ. It is important to note that L, as written, does not contain a conjugate momentum to ϕ, $\partial\phi/\partial t$, which arises by fixing the gauge (for certain choices) [27], and would be necessary in order to develop an integrator in terms of potentials. However, our desired integrators are in terms of gauge invariant fields, and therefore this step is unnecessary (see Section 3). Eqs. (1) and (2) arise from requiring that the action be stationary,

$$\delta\int dt\int d^3x L = 0, \tag{9}$$

where x, y, z, and t are independent variables, and variations are taken with respect to ϕ (and $\partial\phi/\partial t$ for certain gauge choices), each component of $\vec{A}$ and $\partial\vec{A}/\partial t$, and the spatial derivatives that enter into $\vec{\nabla}\phi$ and $\vec{\nabla}\times\vec{A}$.

Marsden and West showed that, given a suitable Lagrangian, it is possible to form a symplectic integration scheme based on a discrete form of the action principle [25]. Their development was in terms of particle Lagrangian mechanics, but it is straightforwardly generalized to a field theory using a Lagrangian density as follows. Eq. (9) is first approximated as

$$\delta \sum_n \int d^3x L_d(n, n+1) = 0, \tag{10}$$

where $L_d(n,n+1)$ is an approximation to the time integral of Eq. (8) over a small time interval, h, from time $t = t_n$ to $t_n + h$,

$$L_d(n, n+1) \approx \int_{t_n}^{t_n+h} dt L. \tag{11}$$

Within each interval, the functions to be varied are ϕ and the components of $\vec{A}$ at times t_n and $t_n + h$, which we will denote by ϕ^n, ϕ^{n+1}, $\vec{A}^n$, and $\vec{A}^{n+1}$, as well as the spatial derivatives that enter into $\vec{\nabla}\phi^n$, $\vec{\nabla}\phi^{n+1}$, $\vec{\nabla} \times \vec{A}^n$, and $\vec{\nabla} \times \vec{A}^{n+1}$. All variations are treated in the standard manner of variational calculus. The components $\vec{A}^n$ and $\vec{A}^{n+1}$ allow $\partial\vec{A}/\partial t$ to be approximated by relating each of component of $\delta\vec{A}^{n+1}$ to $\delta\vec{A}^n$ (and similarly for ϕ for certain gauge choices). Requiring that the variation with respect to A_α be zero, where $\alpha = x$, y, or z, leads to

$$\frac{\delta}{\delta A_\alpha^n} L_d(n, n+1) + \frac{\delta}{\delta A_\alpha^n} L_d(n-1, n) = 0, \tag{12}$$

where variational derivatives are involved,

$$\frac{\delta}{\delta A_\alpha^n} L_d(n, n+1) = \frac{\partial}{\partial A_\alpha^n} L_d(n, n+1) - \sum_\beta \frac{\partial}{\partial \beta} \frac{\partial}{(\partial A_\alpha^n / \partial \beta)} L_d(n, n+1), \tag{13}$$

where $\beta = x$, y, or z. It is not hard to show that Eq. (12) remains satisfied in the course of time iterations $n = 0, 1, \ldots$ if the variables

$$P_\alpha^n = -\frac{\delta}{\delta A_\alpha^n} L_d(n, n+1) \tag{14}$$

and

$$P_\alpha^{n+1} = \frac{\delta}{\delta A_\alpha^{n+1}} L_d(n, n+1), \tag{15}$$

are the discrete momenta canonically conjugate to A_α. Eqs. (14) and (15) can be used to generate SIs, and are analogous to the equations developed by Marsden and West [25], except that they include functional derivatives.

3. Symplectic integrators

SIs can be constructed in many ways using the ideas presented in Section 2 [25]. One method is to choose a form for the discrete Lagrangian, the simplest of which for Eq. (8) is

$$L_d(n, n+1) = h\left\{ \frac{\varepsilon}{2} \left| \frac{\vec{A}^{n+1} - \vec{A}^n}{h} + \vec{\nabla}\phi^{n+1} \right|^2 - \frac{1}{2\mu} |\vec{\nabla} \times \vec{A}^{n+1}|^2 + \vec{J} \cdot \vec{A}^{n+1} - \rho\phi^{n+1} \right\}. \tag{16}$$

The discrete momenta, Eqs. (14) and (15), of $\vec{A}$ are

$$\vec{P}^n = \varepsilon\left(\frac{\vec{A}^{n+1} - \vec{A}^n}{h} + \vec{\nabla}\phi^{n+1} \right), \tag{17}$$

$$\vec{P}^{n+1} = \varepsilon\left\{ \frac{\vec{A}^{n+1} - \vec{A}^n}{h} + \vec{\nabla}\phi^{n+1} \right\} - h\left(\frac{1}{\mu}\vec{\nabla} \times \vec{\nabla} \times \vec{A}^{n+1} - \vec{J} \right), \tag{18}$$

which can be re-arranged to give the update $(\vec{P}^n, \vec{A}^n) \to (\vec{P}^{n+1}, \vec{A}^{n+1})$,

$$\vec{A}^{n+1} = \vec{A}^n + h\left\{ \frac{\vec{P}^n}{\varepsilon} - \vec{\nabla}\phi^{n+1} \right\}, \tag{19}$$

$$\vec{P}^{n+1} = \vec{P}^n - h\left\{ \frac{1}{\mu}\vec{\nabla} \times \vec{\nabla} \times \vec{A}^{n+1} - \vec{J} \right\}. \tag{20}$$

As was noted previously, without gauge fixing [27] an update equation for ϕ cannot be derived from Eq. (16), and thus the SI in Eqs. (19) and (20) is incomplete. However, in terms of gauge invariant fields, a complete SI can be obtained by taking the curl of both sides of Eq. (19) and noting that Eqs. (6) and (17) imply that $\vec{P} = -\varepsilon\vec{E}$,

$$\vec{B}^{n+1} = \vec{B}^n - h\vec{\nabla} \times \vec{E}^n, \tag{21}$$

$$\vec{E}^{n+1} = \vec{E}^n + \frac{h}{\varepsilon}\left(\frac{1}{\mu}\vec{\nabla} \times \vec{B}^{n+1} - \vec{J} \right). \tag{22}$$

It is important to note that, despite the appearance and context of Eqs. (21) and (22), $\vec{E}$ and $\vec{B}$ are not canonically conjugate variables.

Eqs. (21) and (22) represent a simple, first-order accurate in time propagation scheme for Maxwell's equations derived from a discrete Lagrangian approximation to the physically correct Lagrangian density. These equations are similar to the leapfrog method, which is symplectic, often used in FDTD and TD-FEM, except that the fields are not staggered in time. Higher order integration schemes can be constructed using more complex discrete Lagrangians, although they are often implicit. However, discrete Lagrangians can also be combined to give a new discrete Lagrangian of higher order or some other desired property [26,28], from which an explicit SI can be derived. A simple way to do this is to use an explicit symplectic partitioned Runge–Kutta (pRK) method [10,13,14], which we have generalized to describe field theory problems below. In this approach, a given time-step is broken up into r stages, and the canonical variables A and P, which include, but are not limited to the vector potential and conjugate momentum, are updated as

$$A^{j+1} = A^j + hb_j(\partial A/\partial t)^j, \tag{23}$$

$$P^{j+1} = P^j + h\tilde{b}_j(\partial P/\partial t)^{j+1} \tag{24}$$

for $j = 1,\ldots,r$, where

$$(\partial P/\partial t)^j = \frac{\delta}{\delta A^j}L, \tag{25}$$

$$P^j = \frac{\delta}{\delta(\partial A/\partial t)^j}L, \tag{26}$$

and the coefficients b_j and $\tilde{b}_j$ must satisfy certain conditions in order for the pRK method to be symplectic and explicit [13,14]. Note that the time derivative $(\partial A/\partial t)^j$ appearing in Eq. (23) is obtained by solving (the implicit) Eq. (26). The SI in Eqs. (23) and (24) updates the initial values (P^1,A^1) at time t_n to their final values (P^{r+1},A^{r+1}) at time $t_n + h$. The coefficients b_j and $\tilde{b}_j$ exist for any order of accuracy, and have been derived by numerous authors [6–19]. Table 1 shows a small selection of these coefficients.

For the Lagrangian density in Eq. (8), the explicit pRK method is

$$\vec{A}^{j+1} = \vec{A}^j + b_j h\left\{\frac{\vec{P}^j}{\varepsilon} - \vec{\nabla}\phi^{j+1}\right\}, \tag{27}$$

$$\vec{P}^{j+1} = \vec{P}^j - \tilde{b}_j h\left\{\frac{1}{\mu}\vec{\nabla}\times\vec{\nabla}\times\vec{A}^{j+1} - \vec{J}\right\}, \tag{28}$$

from which a discrete Lagrangian for each step can be identified as

$$L_d(j,j+1) = h\left\{\frac{1}{b_j}\frac{\varepsilon}{2}\left|\left(\frac{\vec{A}^{j+1}-\vec{A}^j}{h}\right) + \vec{\nabla}\phi^{j+1}\right|^2 + \tilde{b}_j\left(-\frac{1}{2\mu}|\vec{\nabla}\times\vec{A}^{j+1}|^2 + \vec{J}\cdot\vec{A}^{j+1} - \rho\phi^{j+1}s\right)\right\}. \tag{29}$$

If $r = 1$, Eqs. (27)–(29) are equivalent to Eqs. (16), (19), and (20). For $r \neq 1$, Eqs. (27)–(29) are equivalent to a composition of symplectic Euler steps (SI.1) scaled by b_j and $\tilde{b}_j$, a general result for every explicit symplectic pRK method [13,29]. Again,

Table 1
Select coefficients for the explicit pRK method, Eqs. (23) and (24).

Method	Order	Coefficients	Comments
SI.1	1	$b_1 = 1,\ \tilde{b}_1 = 1$	Symplectic Euler
SI.2	2	$b_1 = 0,\ b_2 = 1,\ \tilde{b}_1 = \tilde{b}_2 = 1/2$	Ruth's symplectic leapfrog[a]
SI.3	3	$b_j = \tilde{b}_{4-j}$ $\tilde{b}_1 = 0.9196615230173999$ $\tilde{b}_2 = 0.25/\tilde{b}_1 - \tilde{b}_1/2,\ \tilde{b}_3 = 1 - \tilde{b}_1 - \tilde{b}_2$	McLachlan and Atela's optimal third-order method[b]
SI.4	4	$b_{7-j} = \tilde{b}_j \quad j = 1,\ldots,6$ $\tilde{b}_1 = 0.2167979108466032$ $\tilde{b}_2 = -0.0283101143283301$ $\tilde{b}_3 = 0.3901418904713324$ $\tilde{b}_4 = -0.2414087476423302$ $\tilde{b}_5 = 0.5908564573813148$ $\tilde{b}_6 = 0.0719226032714098$	Gray and Manolopoulos' fourth-order method[c]

[a] Ref. [8].
[b] Ref. [12].
[c] Ref. [19].

without gauge fixing [27] an update equation for ϕ cannot be derived from Eqs. (27) and (28), but a complete SI in terms of $\vec{E}$ and $\vec{B}$ can be obtained by taking the curl of both sides of Eq. (27) and using the relation $\vec{P} = -\varepsilon\vec{E}$,

$$\vec{B}^{j+1} = \vec{B}^{j} - hb_j\vec{\nabla}\times\vec{E}^{j}, \tag{30}$$

$$\vec{E}^{j+1} = \vec{E}^{j} + h\tilde{b}_j\frac{1}{\varepsilon}\left(\frac{1}{\mu}\vec{\nabla}\times\vec{B}^{j+1} - \vec{J}\right). \tag{31}$$

It is interesting to note that Eqs. (30) and (31) could have been derived by treating $\vec{E}$ and $\vec{B}$ as canonically conjugate variables, and applying the pRK method directly to Eqs. (1) and (2) using a "helicity" Hamiltonian [23], similar to Ref. [20]. However, as noted before, it is very important to realize that $\vec{E}$ and $\vec{B}$ are not canonically conjugate variables with respect to a Hamiltonian that corresponds to the physical energy density. A SI derived on the basis of a "helicity" Hamiltonian is only guaranteed to preserve "helicity", and not the physical dynamical invariants, up to a desired order of accuracy. Only by arriving at Eqs. (30) and (31) using the physically correct Lagrangian density for the electromagnetic field and true canonical variables, $\vec{A}$ and $\partial\vec{A}/\partial t$, have we been able to show that the physical dynamical invariants are preserved. In addition, our approach of developing SIs using the physically correct Lagrangian density allows us to extend these principles to other problems, such as the coupling of quantum mechanics and electrodynamics [24], which typically occurs through a Lagrangian density for the combined system.

4. Numerical stability and dispersion

A fundamental source of error in numerical methods is that waves propagate with a wavelength-dependent velocity, known as numerical dispersion. For spatially discretized domains, the dispersion also depends on the propagation direction [2,30]. In addition, explicit methods are limited to a maximum stable time-step [31], h_{max}. Both of these issues can be analyzed using the von Neumann stability analysis [5], which below we apply to the SIs developed. For simplicity we consider a source free region ($\vec{J} = 0$), and rewrite Eqs. (30) and (31) in matrix form,

$$\begin{bmatrix}\vec{B}^{n+1}\\ \vec{E}^{n+1}\end{bmatrix} = \left(\prod_{j=r}^{1}\begin{bmatrix}[\mathrm{I}] & [0]\\ (h\tilde{b}_j/\varepsilon\mu)[C] & [\mathrm{I}]\end{bmatrix}\begin{bmatrix}[\mathrm{I}] & (-hb_j)[C]\\ [0] & [\mathrm{I}]\end{bmatrix}\right)\begin{bmatrix}\vec{B}^{n}\\ \vec{E}^{n}\end{bmatrix}, \tag{32}$$

where the field vector contains all Cartesian components,

$$\begin{bmatrix}\vec{B}^{n}\\ \vec{E}^{n}\end{bmatrix} = [\,B_x^n \quad B_y^n \quad B_z^n \quad E_x^n \quad E_y^n \quad E_z^n\,]^T. \tag{33}$$

[I] is the 3×3 identity matrix, and [C] is a matrix containing the spatial operations from the curl operator,

$$[C] = \begin{bmatrix}0 & -\partial/\partial z & \partial/\partial y\\ \partial/\partial z & 0 & -\partial/\partial x\\ -\partial/\partial y & \partial/\partial x & 0\end{bmatrix}. \tag{34}$$

It is important to note the order of matrix multiplication in Eq. (32). Eigenmodes of the continuous Eqs. (1) and (2), are assumed to be of the form

$$\begin{bmatrix}\vec{B}^{n}\\ \vec{E}^{n}\end{bmatrix} = \zeta^n\exp[i(k_x x + k_y y + k_z z)]\begin{bmatrix}\vec{B}^{0}\\ \vec{E}^{0}\end{bmatrix}, \tag{35}$$

where k_α ($\alpha = x$, y, or z) are the components of the spatial wavevector, and the time dependence of the mode is contained in the phase factor ζ, which analytically is $\exp(-i\omega h)$, where ω is the angular frequency, and gives information on both the numerical stability and dispersion. Inserting Eq. (35) into (32) and rearranging gives

$$\zeta\begin{bmatrix}\vec{B}^{0}\\ \vec{E}^{0}\end{bmatrix} = \left(\prod_{j=r}^{1}\begin{bmatrix}[\mathrm{I}] & [0]\\ (h\tilde{b}_j/\varepsilon\mu)[\tilde{C}] & [\mathrm{I}]\end{bmatrix}\begin{bmatrix}[\mathrm{I}] & (-hb_j)[\tilde{C}]\\ [0] & [\mathrm{I}]\end{bmatrix}\right)\begin{bmatrix}\vec{B}^{0}\\ \vec{E}^{0}\end{bmatrix}, \tag{36}$$

where

$$[\tilde{C}] = \begin{bmatrix}0 & -f_z & f_y\\ f_z & 0 & -f_x\\ -f_y & f_x & 0\end{bmatrix} \tag{37}$$

and f_α is the result of applying the operations in Eq. (34) on (35), which depends on the spatial discretization. For example, for grid-based central discretizations

$$f_\alpha = 2i\frac{\sin(k_\alpha \Delta\alpha/2)}{\Delta\alpha}. \tag{38}$$

Eq. (36) is an eigenvalue equation with eigenvalues ζ, and while it is possible to solve by hand for low stage numbers, r, the analysis can become quite extensive as r increases, and Maplesoft Maple 9.5 was used to obtain expressions for ζ when $r > 2$.

4.1. Numerical stability

If $|\zeta| > 1$, then the eigenmode, Eq. (35), increases in powers of n, and the method is unstable. Therefore, to find the stability limit Eq. (36) is solved for h with the condition $|\zeta| \leqslant 1$. Numerically, by rearranging the expressions so-obtained for h, it is found, for all SIs discussed, that

$$h \leqslant iC\left(\frac{\varepsilon\mu}{f_x^2 + f_y^2 + f_z^2}\right)^{1/2}, \tag{39}$$

where C is a stability coefficient that depends on the integrator. It is important to note that Eq. (39) appears to be imaginary, but the spatial discretization functions, f_α, are imaginary which makes the expression real. For example, using the SI.2 coefficients and Eq. (38), $C = 2$ and Eq. (39) gives the stability limit of the FDTD method [2]. Stability coefficients for the SIs from Table 1 are shown in Table 2. The high-order integrators are seen to greatly increase the stability limit allowing much larger time steps, with SI.4 giving an increase of $\sim$4.12 times SI.1 and SI.2. However, this increase in stability comes at the expense of increased computational effort (multiple steps), and the efficiencies, in comparison to the single step methods and FDTD, are also shown in Table 2. Even though there is a slight decrease in efficiency, the following section shows there is a great reduction in numerical dispersion.

4.2. Numerical dispersion

After one time-step ($n \to n + 1$), Eq. (35) shows that the phase of the eigenmodes, ζ, will be rotated in the complex plane by an angle determined by ωh. The amount of rotation using numerical methods will differ from the analytical form, with a difference that depends on ω for a fixed h, leading to numerical dispersion. We numerically find, for all the SIs with r-stages that we have considered, that

$$\mathrm{Re}(\zeta) = 1 - \sum_{j=1}^{r} c_j g^j, \tag{40}$$

where c_j are the numerically determined coefficients that depend on the integrator, and

$$g = -\left(\frac{h^2}{\varepsilon\mu}\right)(f_x^2 + f_y^2 + f_z^2). \tag{41}$$

Values of the coefficients for the SIs from Table 1 are shown in Table 3. Considering an exact spatial discretization, so the dispersion due to the SIs alone can be studied, Eq. (41) becomes

$$g = \left(\frac{h^2}{\varepsilon\mu}\right)(k_x^2 + k_y^2 + k_z^2) = \left(\frac{h^2}{\varepsilon\mu}\right)k^2 = (\omega h)^2, \tag{42}$$

where $k = \omega(\varepsilon\mu)^{1/2}$ is the wavevector magnitude. It is important to note that significant additional dispersion arises from the spatial discretization, which can be independent from the time integration method, such as intrinsic velocity anisotropy in FDTD [30]. From Eq. (42), it is seen that Eq. (40) is essentially a truncated Taylor expansion for $\cos(\omega h)$, which is the analytical form of $\mathrm{Re}(\zeta)$ in Eq. (35). Fig. 1 shows Eq. (40) and $\cos(\omega h)$ plotted over the range $0 \leqslant \omega h \leqslant \pi$ for the SIs in Table 1. High numerical dispersion is seen to occur using the low-order SIs, SI.1 and SI.2, especially for high ω, which is seen to significantly decrease by using the high-order SIs. Calculated values of the maximum and average errors of each SI are shown

Table 2
Stability coefficients for Eq. (39), and the efficiency in comparison to SI.1. The FDTD method is included in this table as discussed in the text.

Method	Stability coefficient (C)	Number of full steps	Efficiency
FDTD	2.000000000	1.0	1.000
SI.1	2.000000000	1.0	1.000
SI.2	2.000000000	1.0	1.000
SI.3	4.520089519	3.0	0.753
SI.4	8.240410106	6.0	0.687

Table 3
Coefficients for Eq. (40), and the maximum and average errors associated with the SIs rotation of the real part of the eigenmode phase compared to the analytical form, $\cos(\omega h)$, over the range $0 \leqslant \omega h \leqslant \pi$.

Method	Coefficients (c_j)	Max. error (%)	Average error (%)
SI.1	$c_1 = -0.5$	293.47939	32.53317
SI.2	$c_1 = -0.5$	293.47939	32.53317
SI.3	$c_1 = -0.5$ $c_2 = 0.041\bar{6}$ $c_3 = -0.001076073122$	8.93847	0.96005
SI.4	$c_1 = -0.5$ $c_2 = 0.041\bar{6}$ $c_3 = -0.001365305423$ $c_4 = 0.00002133566312$ $c_5 = -0.0000001495359056$ $c_6 = 0.0000000003017236690$	0.00393	0.02687

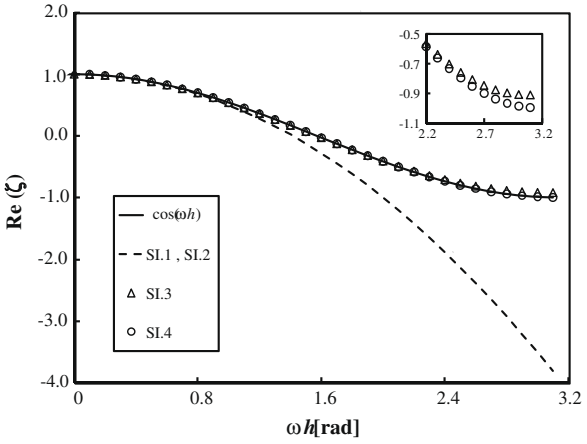

Fig. 1. SI rotation of the real part of the eigenmode phase after a single time-step in comparison to the analytical form, $\cos(\omega h)$, over the range $0 \leqslant \omega h \leqslant \pi$. The inset shows an expanded view of the high ωh region.

in Table 3, where for example, it is seen that the average error using SI.4 is only 0.027% compared to 32.533% with SI.1 and SI.2.

5. Practical implementation using FDTD techniques

For the SIs to be practically useful, the spatial domain must be discretized, boundary conditions must be applied, and initial waves of arbitrary form must be easily introduced into the system. These are extremely important issues that are often not considered when new numerical approaches for solving Maxwell's equations are developed. The modern forms of the FDTD method [2] effectively deal with these issues, thus accounting for its continued popularity. In this section, we describe how such techniques can be used for implementation of our integrators.

5.1. Spatial discretization

For a numerically accurate solution, it is crucial that the spatial discretization allows $\vec{E}$ and $\vec{B}$ to satisfy Eqs. (3) and (4), as well as the appropriate boundary conditions across material interfaces. One suitable discretization is with the Yee spatial lattice [1], where $\vec{E}$ and $\vec{B}$ circulate each other on a Cartesian grid, and the spatial derivatives are approximated using Taylor expansions.

5.2. Boundary conditions

Even when simulating infinite domains, the computational domain must be truncated. However, many techniques have been developed to mimic open regions of space. One of the most successful techniques is to truncate the domain with artificial materials that absorb nearly all incident waves, called perfectly matched layers (PML) [32], which simulate an infinite extent along the truncation direction. Neglecting reflection errors from the PML [2], the interior numerical solution (i.e. not

inside the PML) is unaffected. An efficient and accurate way of implementing PML with the Yee spatial lattice is to use convolutional PML (CPML) [33].

The implementation of CPML involves stretching the spatial derivatives in the curl operators and superimposing time-dependent functions, $\vec{\Phi}$ and $\vec{\Psi}$, onto them. In a region of CPML, Eqs. (30) and (31) become

$$\vec{B}^{j+1} = \vec{B}^{j} - h\tilde{b}_j(\vec{\nabla}_s \times \vec{E}^{j} + \vec{\Phi}^{j}), \tag{43}$$

$$\vec{E}^{j+1} = \vec{E}^{j} + h\tilde{b}_j \frac{1}{\varepsilon}\left(\frac{1}{\mu}\vec{\nabla}_s \times \vec{B}^{j+1} + \vec{\Psi}^{j+1} - \vec{J}\right), \tag{44}$$

where $\vec{\nabla}_s\times$ is a curl operator with stretched spatial derivatives,

$$\vec{\nabla}_s \times \vec{F} = \hat{x}\left(\frac{1}{\kappa_y}\frac{\partial F_z}{\partial y} - \frac{1}{\kappa_z}\frac{\partial F_y}{\partial z}\right) + \hat{y}\left(\frac{1}{\kappa_z}\frac{\partial F_x}{\partial z} - \frac{1}{\kappa_x}\frac{\partial F_z}{\partial x}\right) + \hat{z}\left(\frac{1}{\kappa_x}\frac{\partial F_y}{\partial x} - \frac{1}{\kappa_y}\frac{\partial F_x}{\partial y}\right), \tag{45}$$

where κ_α ($\alpha = x, y,$ or z) is a scaling factor that increases from 1 at $\alpha = 0$ to $\kappa_{\alpha,max}$ at $\alpha = d_\alpha$, where d_α is the depth of the CPML in the α-direction. Various formulas exist for κ_α [2], one of the most successful being polynomial grading with CPML depth [34],

$$\kappa_\alpha = 1 + (\kappa_{\alpha,max} - 1)\left(\frac{\alpha}{d_\alpha}\right)^m \tag{46}$$

where m is the polynomial order. The functions $\vec{\Phi}$ and $\vec{\Psi}$ are given by

$$\vec{\Phi} = \hat{x}(\Phi_{x,y,z} - \Phi_{x,z,y}) + \hat{y}(\Phi_{y,z,x} - \Phi_{y,x,z}) + \hat{z}(\Phi_{z,x,y} - \Phi_{z,y,x}), \tag{47}$$

$$\vec{\Psi} = \hat{x}(\Psi_{x,y,z} - \Psi_{x,z,y}) + \hat{y}(\Psi_{y,z,x} - \Psi_{y,x,z}) + \hat{z}(\Psi_{z,x,y} - \Psi_{z,y,x}), \tag{48}$$

and are updated by the equations

$$\Phi^{j+1}_{\alpha,\beta,\gamma} = w_{1,\alpha}\Phi^{j}_{\alpha,\beta,\gamma} + w_{2,\alpha}\frac{\partial}{\partial\beta}E^{j+1}_{\gamma}, \tag{49}$$

$$\Psi^{j+1}_{\alpha,\beta,\gamma} = w_{1,\alpha}\Psi^{j}_{\alpha,\beta,\gamma} + w_{2,\alpha}\frac{1}{\mu}\frac{\partial}{\partial\beta}B^{j+1}_{\gamma}, \tag{50}$$

where α, β, $\gamma = x, y,$ or z, and

$$w_{1,\alpha} = \exp\left[-\left(\frac{\sigma_\alpha}{\varepsilon_0\kappa_\alpha} + \frac{a_\alpha}{\varepsilon_0}\right)\Delta h\right], \tag{51}$$

$$w_{2,\alpha} = \frac{\sigma_\alpha}{\sigma_\alpha\kappa_\alpha + \kappa_\alpha^2 a_\alpha}(w_{1,\alpha} - 1), \tag{52}$$

where $\Delta h = h\tilde{b}^j$ for the coefficients in Eq. (49) and $\Delta h = hb^j$ for the coefficients in Eq. (50). Polynomial gradings for σ_α and a_α are given by

$$\sigma_\alpha = \sigma_{\alpha,max}\left(\frac{\alpha}{d_\alpha}\right)^m, \tag{53}$$

$$a_\alpha = a_{\alpha,max}\left(1 - \frac{\alpha}{d_\alpha}\right)^{m_a}, \tag{54}$$

where the polynomial order m_a is independent from m. Eqs. (53) and (54) show that σ_α increases from 0 at $\alpha = 0$ to $\sigma_{\alpha,max}$ at $\alpha = d_\alpha$, and a_α decreases from $a_{\alpha,max}$ at $\alpha = 0$ to 0 at $\alpha = d_\alpha$. Optimum parameters for d_α, m, m_a, κ_α, σ_α, and a_α are simulation dependent, but for general FDTD simulations effective parameters have been found to be $d_\alpha \approx 10\Delta\alpha$, $m = 3$ or 4, $m_a = 1$, $7 < \kappa_{\alpha,max} < 20$, $0.15 < a_{\alpha,max} < 0.3$, and $0.8\sigma_{\alpha,\mathrm{opt}} < \sigma_{\alpha,max} < 1.4\sigma_{\alpha,\mathrm{opt}}$ [2,34], where

$$\sigma_{\alpha,\mathrm{opt}} \approx \frac{0.8(m+1)}{\Delta\alpha}\left(\frac{\varepsilon_0}{\varepsilon_{r,\mathrm{eff}}\mu_{r,\mathrm{eff}}\mu_0}\right)^{1/2}, \tag{55}$$

$\Delta\alpha$ is the grid spacing in the α-direction, and $\varepsilon_{r,\mathrm{eff}}$ and $\mu_{r,\mathrm{eff}}$ are the effective relative permittivity and permeability of the CPML (e.g. the mean values). For a complete discussion of CPML, including derivations of Eqs. (43)–(55), see Refs. [2,33].

5.3. Initial conditions

Given suitable initial conditions defined everywhere in the computational domain, the SIs will properly evolve the fields according to Eqs. (1) and (2). However, defining computational domains for initial conditions with large spatial extent is often inefficient and unnecessary. A more efficient technique to introduce fields into the computational domain, particularly with the Yee spatial lattice, is to use the total field–scattered field (TF–SF) technique [35–37]. The implementation of this involves splitting the computational domain into two regions, an interior total field region and an exterior scattered field

region. The SIs can be used directly in each region without modification. However, near the boundaries, where the spatial derivatives extend into both regions, the fields are modified using the (known) incident field, so that all equations are consistent.

6. Numerical examples

In this section, we present numerical examples that demonstrate that the validity of the FDTD implementation techniques and that the high-order SIs do efficiently reduce the numerical dispersion. We first consider a calculation of the scattering cross-section of a 100 nm radius infinite cylinder in the xy-plane with a refractive index of $n = 3.0$ illuminated with TE_z polarized light (i.e. the magnetic field is transverse to the xy-plane) in comparison to the analytical Mie theory result. A two-dimensional computational domain 300×300 nm was discretized using the Yee spatial lattice with grid spacings of $\Delta x = \Delta y = 1$ nm, and terminated with 20 layers of CPML. Spatial derivatives were approximated using second-order accurate Taylor expansions. A Gaussian-damped sinusoidal pulse traveling in the $+x$-direction,

$$\exp\left(-\frac{[t-(x-x_0)/c]^2}{2\sigma^2}\right)\sin(\omega_0 t), \tag{56}$$

where σ is the width of the damping, x_0 is the center position of the pulse at $t = 0$, and ω_0 is the center angular frequency, was introduced into the computational domain using the TF–SF technique. The parameters in Eq. (56) were chosen such that the pulse had wavelength content over the range of interest ($\lambda = 350$–1000 nm): $\sigma = 0.11$ fs and $\omega_0 = 600$ nm. The scattering cross-section was calculated by integrating the normal component of the Poynting vector around a closed surface encompassing the cylinder using the frequency-domain scattered fields, which were obtained by Fourier transforming the time-domain fields for 100 fs. The result calculated using SI.4 with $h = 0.99h_{max}$ is shown in Fig. 2, where very accurate results are seen. Fig. 2 is not meant to imply that the other SIs give significantly less accurate results (see below for a detailed comparison), but rather that the FDTD implementation techniques work.

In order to demonstrate the ability of the high-order SIs to efficiently reduce numerical dispersion, we compared the analytical propagation of a narrow Gaussian pulse to the numerical result over a long distance. A 400 μm one-dimensional computational domain was discretized using the Yee spatial lattice with grid spacings of $\Delta x = 5$ nm. Spatial derivatives were again approximated using second-order accurate Taylor expansions. A Gaussian pulse traveling in the $+x$ direction,

$$E_y(t,x) = \exp\left(-\frac{[t-(x-x_0)/c]^2}{2\sigma^2}\right), \tag{57}$$

$$B_z(t,x) = \frac{1}{c}\exp\left(-\frac{[t-(x-x_0)/c]^2}{2\sigma^2}\right), \tag{58}$$

was inserted into the computational domain by specifying initial values of E_y and B_z, Eqs. (57) and (58), everywhere with t=0, x_0=200 μm, and $\sigma = 0.025$ fs, chosen such that the pulse contained wavelength content down to ~60 nm where extremely high numerical dispersion was expected to occur. The simulation was stopped after 500 fs, upon which time the pulse had only propagated ~150 μm, and therefore no boundary truncation (e.g. CPML) was necessary. For all t, E_y and B_z are theoretically specified everywhere in the computational domain by Eqs. (57) and (58). However, because of numerical dispersion,

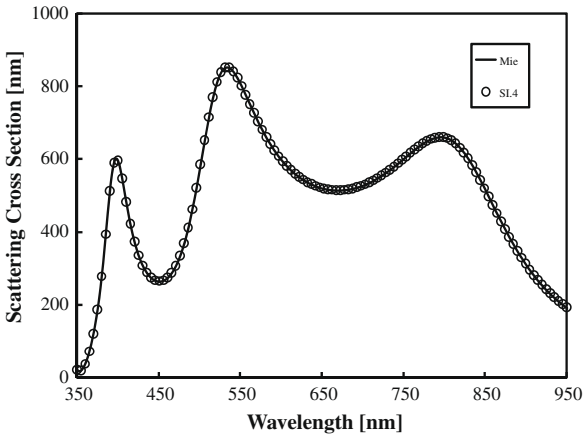

Fig. 2. Scattering cross-section of a 100 nm radius infinite cylinder with refractive index $n = 3.0$ calculated with SI.4, implemented using FDTD techniques, in comparison to the analytical Mie theory result.

not all wavelength components of the pulse will propagate at the same speed, and thus over time its structure will deform. In order to measure this deformation we looked at the energy of the error between the analytical and numeric pulses,

$$\int \frac{1}{2}\left(\varepsilon(E_y^n(x) - E_y(nh,x))^2 + \frac{1}{\mu}(B_z^n(x) - B_z(nh,x))^2\right)dx. \tag{59}$$

For the discretization under consideration, Eq. (59) becomes

$$\Delta x \sum_{l=1}^{L} \frac{1}{2}\left(\varepsilon(E_y^n(l\Delta x) - E_y(nh,l\Delta x))^2 + \frac{1}{\mu}(B_z^n(l\Delta x) - B_z(nh,l\Delta x))^2\right), \tag{60}$$

where L is the number of grid points. Absolute errors normalized by the incident energy with $h = 0.95h_{max}$ for all of the SIs discussed are shown in Fig. 3(a). It should be noted that measurements began after the pulse had propagated 10 fs to avoid numerical errors associated the initial conditions (e.g. evanescent and $-x$ directed wave components). For all SIs, the error is seen to increase over time, as expected, and those associated with SI.3 and SI.4 are less than half that of SI.1 and SI.2. It is interesting to observe what happens when $h \ll h_{max}$. This may correspond to a simulation with an inhomogeneous computational domain, where h_{max} differs by region. Fig. 3(b) shows the same situation as Fig. 3(a), except with $h = 0.5h_{max}$. The errors associated with SI.1 and SI.2 are seen to dramatically decrease, whereas those of SI.3 and SI.4 remain relatively the same (although still below SI.1 and SI.2). The high-order integrators are therefore particularly well-suited for maintaining a minimal amount numerical dispersion in inhomogeneous computational domains. In order to directly compare the SIs, the errors relative to the single step method (SI.1) were calculated, Fig. 4(a). As expected from Fig. 3, the error of SI.2 is almost identical to SI.1, whereas SI.3 and SI.4 have significantly less. In addition, although hard to discern from Fig. 4, the relative errors of SI.3 and SI.4 decrease over time. Multiplying the results in Fig. 4(a) by the efficiency in Table 2 gives an idea of the error per computational effort, Fig. 4(b), and demonstrates that the high-order SIs efficiently minimize numerical dispersion.

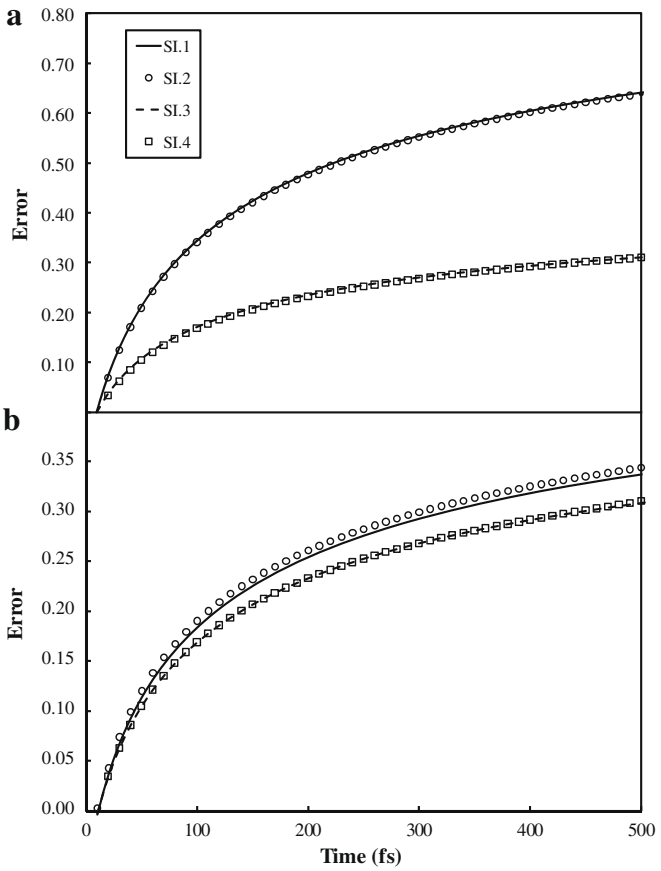

Fig. 3. Energy of the error relative to the incident energy as a function of time in the propagation of a one-dimensional Gaussian pulse for 500 fs for each SI with (a) $h = 0.95h_{max}$ and (b) $h = 0.5h_{max}$.

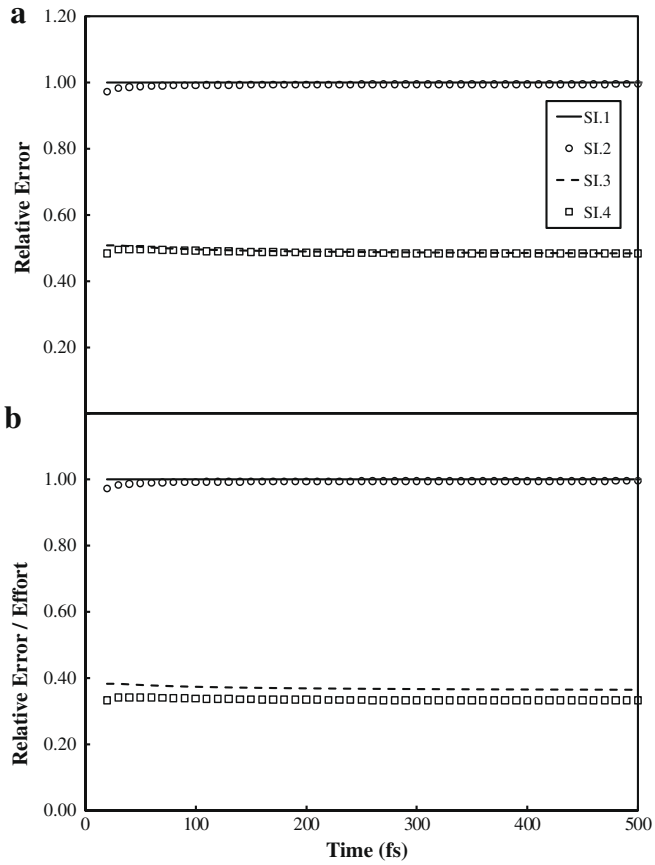

Fig. 4. (a) Energy of the error as a function of time in the propagation of a one-dimensional Gaussian pulse for 500 fs for each SI relative to SI.1 with $h = 0.95h_{max}$. (b) Error per computational effort.

7. Summary and conclusions

A discrete action principle for electrodynamics was derived, which was then used to construct explicit symplectic integrators for Maxwell's equations. The physically correct electrodynamics Lagrangian density, involving the vector and scalar potentials, was used for our formulation, but it was demonstrated that the integrators could all be expressed entirely in terms of the electric and magnetic fields. By combining discrete Lagrangians in an explicit symplectic partitioned Runge–Kutta method, an integrator capable of achieving any order of accuracy was obtained. The numerical stability was shown to be greatly increased and the numerical dispersion greatly decreased, compared to other methods, by using the high-order integrators. Numerical examples were presented that demonstrate this, especially as the time-step is decreased from the maximum stable time-step. These integrators are therefore particularly well suited for modeling the propagation of electromagnetic waves in inhomogeneous computational domains. We demonstrated that the integrators can be used along with a lot of the standard embellishments of the finite-difference time-domain method, which were used for our numerical examples. However, the integrators are not limited to a finite-difference method, and we are currently implementing them using a finite element approach.

The integrators presented here do not explicitly allow for dispersive materials, which would involve additional current or polarization terms that would be coupled to the electric field. However, such behavior can be incorporated with our integrators using a split-operator approach as used in Ref. [38], and we are currently investigating this and other approaches for modeling these materials.

We are currently using the ideas presented here to construct symplectic integrators for other approaches in physics that are based on Lagrangian mechanics, such as the Car–Parrinello molecular dynamics method [39] and time-domain density functional theory [40].

Acknowledgments

G.C.S. and J.M.M. were supported by the US Department of Energy under Grant No. DEFG02-03-ER15487 and the Northwestern Materials Research Center, sponsored by the National Science Foundation (DMR-0520513). The work at Argonne

National Laboratory was supported by the US Department of Energy, Basic Energy Sciences, under Contract No. DE-AC02-06CH11357. The authors thank David Masiello for many fruitful discussions.

References

[1] K.S. Yee, Numerical solution of initial boundary value problems involving Maxwell's equations in isotropic media, IEEE Trans. Antennas Propagat. AP-14 (1966) 302–307.
[2] A. Taflove, S. Hagness, Computational Electrodynamics: The Finite-Difference Time-Domain Method, third ed., Artech House, MA, 2005.
[3] J. Jin, The Finite Element Method in Electromagnetics, second ed., Wiley, New York, 2002.
[4] C.W. Manry, S.L. Broschat, J.B. Schneider, Higher-order FDTD methods for large problems, J. Appl. Comput. Electromagnet. Soc. 10 (1995) 17–29.
[5] W.H. Press, B.P. Flannery, S.A. Teukolsky, W.T. Vetterling, Numerical Recipes, Cambridge University, New York, 1986.
[6] L. Verlet, Computer experiments on classical fluids. I: Thermodynamical properties of Lennard-Jones molecules, Phys. Rev. 159 (1967) 98–103.
[7] H. Goldstein, Classical Mechanics, second ed., Addison-Wesley, MA, 1980.
[8] R.D. Ruth, A canonical integration technique, IEEE Trans. Nucl. Sci. NS-30 (1983) 2669–2671.
[9] H. Yoshida, Construction of higher order symplectic integrators, Phys. Lett. A 150 (1990) 262–268.
[10] Y.B. Suris, Hamiltonian methods of Runge–Kutta type and their variational interpretation, Math. Model. 2 (1990) 78–87 (in Russian).
[11] J. Candy, W. Rozmus, A symplectic integration algorithm for separable Hamiltonian functions, J. Comput. Phys. 92 (1991) 230–256.
[12] R.I. McLachlan, P. Atela, The accuracy of symplectic integrators, Nonlinearity 5 (1992) 541–562.
[13] D.I. Okunbor, R.D. Skeel, Explicit canonical methods for Hamiltonian systems, Math. Comput. 59 (1992) 439–455.
[14] J.M. Sanz-Serna, The numerical integration of Hamiltonian systems, in: J.R. Cash, I. Gladwell (Eds.), Computational Ordinary Differential Equations, Clarendon Press, Oxford, 1992, pp. 437–449.
[15] M. Tuckerman, B.J. Berne, G.J. Martyna, Reversible multiple time scale molecular dynamics, J. Chem. Phys. 97 (1992) 1990–2001.
[16] M.P. Calvo, J.M. Sanz-Serna, The development of variable-step symplectic integrators with, applications to the two-body problem, SIAM J. Sci. Comput. 14 (1993) 936–952.
[17] J.M. Sanz-Serna, M.P. Calvo, Numerical Hamiltonian Problems, Chapman and Hall, London, 1993.
[18] S.K. Gray, D.W. Noid, B.G. Sumpter, Symplectic integrators for large scale molecular dynamics simulations: a comparison of several explicit methods, J. Chem. Phys. 101 (1994) 4062–4072.
[19] S.K. Gray, D.E. Manolopoulos, Symplectic integrators tailored to the time-dependent Schrodinger equation, J. Chem. Phys. 104 (1996) 7099–7112.
[20] I. Saitoh, Y. Suzuki, N. Takahashi, The symplectic finite difference time domain method, IEEE Trans. Magn. 37 (2001) 3251–3254.
[21] Z. Huang, X. Wu, Symplectic partitioned Runge–Kutta scheme for Maxwell's equations, Int. J. Quant. Chem. 106 (2005) 839–842.
[22] W. Sha, Z. Huang, X. Wu, M. Chen, Application of the symplectic finite-difference time-domain scheme to electromagnetic simulation, J. Comput. Phys. 225 (2007) 33–50.
[23] N. Anderson, A.M. Arthurs, A variational principle for Maxwell's equations, Int. J. Electron. 45 (1978) 333–334.
[24] D. Masiello, E. Deumens, Y. Öhrn, Dynamics of an atomic electron and its electromagnetic field in a cavity, Phys. Rev. A 71 (2005) 032108.
[25] J.E. Marsden, M. West, Discrete mechanics and variational integrators, Acta Numer. 10 (2001) 357–514.
[26] H. Qin, X. Guan, Variational symplectic integrator for long-time simulations of the guiding-center motion of charged particles in general magnetic fields, Phys. Rev. Lett. 100 (2008) 035006.
[27] J.D. Jackson, Classical Electrodynamics, third ed., Wiley, New York, 1998.
[28] R.I. McLachlan, S.K. Gray, Optimal stability polynomials for splitting methods, with application to the time-dependent Schrodinger equation, Appl. Numer. Math. 25 (1997) 275–286.
[29] E. Hairer, C. Lubich, G. Wanner, Geometric Numerical Integration: Structure-preserving Algorithms for Ordinary Differential Equations, Springer, Berlin, 2002.
[30] Y. Liu, Fourier analysis of numerical algorithms for the Maxwell's equations, J. Comput. Phys. 124 (1996) 396–416.
[31] J. Hoffman, Numerical Methods for Engineers and Scientists, McGraw-Hill, New York, 1992.
[32] J.P. Berenger, A perfectly matched layer for the absorption of electromagnetic waves, J. Comput. Phys. 114 (1994) 185–200.
[33] J.A. Roden, S.D. Gedney, Convolutional PML (CPML): an efficient FDTD implementation of the CFS-PML for arbitrary media, Microwave Opt. Tech. Lett. 27 (2000) 334–339.
[34] J.P. Berenger, Perfectly matched layer for the FDTD solution of wave–structure interaction problems, IEEE Trans. Antennas Propagat. 51 (1996) 110–117.
[35] D.E. Merewether, R. Fisher, F.W. Smith, On implementing a numeric Huygen's source scheme in a finite difference program to illuminate scattering bodies, IEEE Trans. Nucl. Sci. 27 (1980) 1829–1833.
[36] G. Mur, Absorbing boundary conditions for the finite-difference approximation of the time-domain electromagnetic field equations, IEEE Trans. Electromagnet. Comp. 23 (1981) 377–382.
[37] K.R. Umashankar, A. Taflove, A novel method to analyze electromagnetic scattering of complex objects, IEEE Trans. Electromagnet. Comp. 24 (1982) 397–405.
[38] A.G. Borisov, S.V. Shabanov, Lanczos pseudospectral method for initial-value problems in electrodynamics and its applications to ionic crystal gratings, J. Comput. Phys. 209 (2005) 643–664.
[39] R. Car, M. Parrinello, Unified approach for molecular dynamics and density-functional theory, Phys. Rev. Lett. 55 (1985) 2471–2474.
[40] E. Runge, E.K.U. Gross, Density-functional theory for time-dependent systems, Phys. Rev. Lett. 52 (1984) 997.